Int. J. Nonlinear Anal. Appl. In Press, 1–16
ISSN: 2008-6822 (electronic)
http://dx.doi.org/10.22075/ijnaa.2024.35039.5233

Optimizing airflow in operating rooms to reduce the risk of airborne infections

Koorosh Aminian

Department of Mechanical Engineering, Shahid Bahonar University of Kerman, Kerman, Iran

(Communicated by Seyed Hossein Siadati)

Abstract

This study examines the impact of airflow patterns, resulting from various directions of fan coil air outlets, on the distribution of pollutant particles in an operating room. The sample space was modeled using the Eulerian-Lagrangian method and validated against existing data. The turbulent airflow in a 49-cubic-meter operating room, equipped with a floor-mounted fan coil, was simulated using Computational Fluid Dynamics (CFD) with OpenFOAM and the BuoyantBoussinesqPimpleFoam solver. The room's airflow was measured at 4160 cubic meters per hour for incoming air and 4056 cubic meters per hour for outgoing air, with 5 exhaust vents and 4 supply vents. Results indicated that pollutant concentrations decreased with increasing height. At 1.2 meters above the floor, the concentration of suspended particles was approximately 20% lower than at floor level. Smaller particles, less than 5 microns, were less likely to settle due to reduced gravitational forces and were more effectively removed by the ventilation system. This system successfully eliminated over 85% of airborne pollutants from the operating room, demonstrating its effectiveness in maintaining a clean and safe environment.

Keywords: airflow optimization, operating room, airborne infections, computational fluid dynamics, HVAC system, geothermal heating
2020 MSC: 90C24

1 Introduction

In today's world, many modern industries require environments free of particle contamination and bacteria, particularly in cleanroom settings. HVAC (Heating, Ventilation, and Air Conditioning) systems are the primary tools for creating a safe and comfortable environment by maintaining air quality and eliminating pollutants within indoor spaces [15]. A cleanroom is a controlled environment where parameters such as airborne particle count, temperature, humidity, air pressure, and airflow patterns are regulated [16]. Air pollution from both internal and external sources has a significant impact on air quality and human health. In the past, researchers recognized that dust could be harmful, but they did not establish a precise link between respiratory diseases and dust inhalation. At that time, little research had been conducted on the effects of indoor air quality on comfort and well-being [12]. Currently, to improve indoor air quality, in addition to using standard air distribution and HVAC systems to reduce pollutants, simpler methods like regular carpet cleaning have gained attention [7]. The U.S. Environmental Protection Agency (EPA) provides guidelines for cleaning based on factors such as traffic, number of family members, pets, children, and

---

Email address: `koorosh.aminian74@gmail.com` (Koorosh Aminian)

Received: June 2024 *Accepted:* September 2024

smokers. Moreover, the ventilated air in indoor spaces must be free of contaminants at hazardous concentration levels to ensure comfort and well-being for most individuals [14].

In operating rooms, precise environmental control is critical for ensuring patient safety and the success of surgical procedures [2]. One of the most significant challenges in this context is managing and optimizing airflow to prevent airborne infections that can lead to serious complications for patients [6]. Studies on various hospital staff indicate that operating room personnel are at a higher risk of exposure to various hazards and diseases compared to other hospital departments [17]. A primary reason for this is the failure to adhere to professional hygiene standards by operating room staff. For instance, contact with blood and the subsequent risk of contracting diseases like hepatitis and AIDS, which are bloodborne, often occur due to negligence and poor personal and workplace hygiene [9]. Additionally, other factors contribute to the increased vulnerability of operating room staff, which are not related to individual behavior. Examples include the release of anesthetic gases into the environment and poor air quality in the operating room, which are associated with hospital equipment and ventilation systems [4].

Lewis [11] investigated the impact of air distribution in operating rooms on the infection rates within these environments, concluding that an optimized air distribution system plays a crucial role in maintaining the proper conditions in the operating room [11]. In the field of operating room HVAC systems, “Blower” and “Crow” are considered pioneers. In 1691, they attempted to design a clean room with a downward piston airflow, where the air was expelled through distribution filters covering the entire ceiling. However, due to the heat generated by individuals, the presence of lamps in the operating room, and the low speed of the airflow, creating a suitable direct airflow was impossible [5]. The advancement of computational fluid dynamics (CFD) in the numerical modeling of operating room HVAC systems was initiated by Andrew Spalding in early 1691 [16]. Conventional air distribution and HVAC systems in operating rooms become fully satisfactory only when proper design and protection of the operating room are also in place. Effective control of airborne particles, hazardous chemicals, radioactive substances, odors, viruses, and microorganisms that are transmitted through the air is of paramount importance for individuals within the room [8].

Given the importance of cleanliness and environmental control in operating rooms, optimizing airflow to reduce the risk of airborne infections is a key challenge. The appropriate airflow in operating rooms must be capable of removing or reducing suspended particles and microbial contaminants from the environment to minimize the risk of infection [3]. However, designing and adjusting HVAC systems to ensure that all areas of the room are uniformly ventilated, and that airflow is managed in such a way that sensitive areas near the patient are adequately protected, is a complex task [6]. Currently, many operating rooms use traditional air ventilation systems, which may not fully address all environmental challenges. Optimizing these systems requires a deep understanding of how airflow distribution impacts contamination and suspended particles [7]. Research on optimizing airflow in operating rooms to reduce the risk of airborne infections is of particular importance. The primary reason for the significance of this research is the health and safety of patients. Airborne infections can significantly affect the outcome of surgical procedures and increase treatment costs. By optimizing airflow, the risk of these infections can be reduced, improving the quality and effectiveness of surgeries [5]. Additionally, optimizing airflow can help reduce hospital costs and financial resources associated with additional treatments and prolonged patient stays. This research can also contribute to the design and improvement of HVAC systems, setting new standards for operating rooms that enhance safety and quality in healthcare services [11].

The present study investigates the effect of airflow patterns, resulting from different directions of fan coil air outlets, on the distribution of pollutants in an operating room while maintaining thermal comfort conditions. The modeling of the sample space is carried out using the Eulerian-Lagrangian method and validated against existing experimental and numerical data. For solving the equations, the turbulent air flow in a sample space equipped with a floor-standing fan coil was initially calculated using computational fluid dynamics (CFD) and OpenFOAM software, along with the Buoyant Boussinesq solver. Then, using the obtained velocity distribution and the PIMPLE solver package, the movement of pollutants in the Lagrangian view was examined. This study also explores a new ventilation system with minimal energy consumption, where the energy required for building ventilation is sourced from geothermal heat. The main objectives of this research include modeling airflow, temperature, and particle dispersion in the operating room, determining the dimensions of underground channels for maximizing the use of geothermal cooling, and analyzing the comfort conditions in the operating room. Numerical solution methods will be used to solve the flow and energy equations to analyze the system’s performance. To ensure the accuracy of the calculations, comparisons will be made with previous work in the areas of airflow and particle movement, and important exergy and energy indicators such as coefficient of performance, exergy loss, exergy loss ratio, exergy loss coefficient, exergy efficiency, and thermodynamic perfection degree will be examined.

2 Methodology

2.1 Execution technique

The $k-\varepsilon$ standard model, known for its simplicity and accuracy, was used in this study with FLUENT software to simulate turbulent airflow in a cylindrical inlet. The simulation aimed to predict velocity and pressure distribution within the pipe and analyze the impact of the Reynolds number on flow structure. Boundary conditions included uniform inlet velocity, constant outlet pressure, and smooth, non-slip walls. A dense unstructured mesh was used near the walls, and the results, including axial velocity profiles, were compared with experimental data. The specifications of the examined operating rooms are given in table 1 and the specifications of the incoming particles in table 2.

Table 1: Specifications of the Operating Rooms Under Investigation

Performance parameters	Number of inlets	Number of outlets	Inlet airflow	Outlet airflow	Operating room volume	Air distribution rate per hour
B	4	5	4160	4056	49	85
C	4	3	2120	2203	43	49
D	4	6	2880	3036	65	45

Table 2: Specifications of Inlet Particles

Specifications	Value
Particle Emission Rate	2,760,000 particles per minute
Mean Diameter of Emitted Particles	0.1 - 0.75 - 4 micrometers
Particle Density	2000 kg/m^3
Particle Release Location	All 150- and 200-millimeter vents

2.2 Assumptions for modeling and analysis

In this study, the following assumptions were used for simulating flow and particles: The fluid under investigation is considered to be compressible and dry air. The viscosity and thermal conductivity of the fluid are assumed to be constant. The flow is modeled as three-dimensional, turbulent, and steady-state. The effect of gravity is considered, while surface-to-surface radiation effects are neglected.

2.3 Governing equations

In the current research, the governing equations for fluids are solved using a discrete method via algebraic equations for meshes created by dividing the computational domain. The velocity, pressure, and temperature fields in the region of interest are obtained. Using the results from solving these equations, the resultant forces on surfaces, drag and lift coefficients, and heat transfer coefficients can be calculated [20].

$$\rho(\text{pressure}, \text{temperature}) = \text{Density} \tag{2.1}$$

The viscosity (μ) and thermal conductivity (k) of the fluid are assumed to be constant.

$$\text{constant} = \text{constant} \qquad k = \mu \tag{2.2}$$

The flow is considered to be three-dimensional, turbulent, and steady-state.

$$0 = (\text{Flow properties})\frac{\partial}{t\partial} \tag{2.3}$$

The effect of gravity (g) is considered, while surface-to-surface radiation effects are neglected.

$$0 = g \text{ Radiative heat transfer} \cdot \rho = \text{Gravity force}$$

2.3.1 Governing equations for solid particle motion

To accurately predict particle transport, it is essential to consider all factors affecting particle motion and displacement. The most significant factors influencing solid particle transport include:

1) Hydrodynamic Force and Particle Weight
2) Particle Interaction with Solid Boundaries
3) Effect of Flow Turbulence on Particle Movement and Dispersion

Forces acting on particles include both volumetric and surface forces. The only volumetric force affecting particle transport is the weight of the particles. Assuming that all particles are spherical, the effective weight of the particles is calculated using the following equation [22, 23]:

$$W = m_p g = (p_p - p_f)\left(\frac{\pi d_p^3}{6}\right) g \tag{2.4}$$

where ρ_p is the particle density and ρ_f is the fluid density.

2.3.2 Continuity equation

One of the fundamental principles of fluid mechanics is the principle of mass conservation, which states that mass is neither created nor destroyed. This principle is expressed by the continuity equation, which for compressible fluids is given by:

$$\frac{\partial(\rho)}{\partial t} + \nabla \cdot (\rho u) = 0 \tag{2.5}$$

where, ρ is the fluid density, t is time, u is the velocity vector, and ∇ represents the divergence operator. For incompressible fluids, where the density is constant, the continuity equation simplifies to:

$$\nabla \cdot u = 0 \tag{2.6}$$

2.4 Governing equations for the continuous phase

In the study of multiphase flows, particularly those involving a continuous phase and a dispersed phase, the governing equations for the continuous phase are typically derived from the Navier-Stokes equations or other conservation laws to describe the fluid dynamics. The continuous phase generally dominates the system, with the dispersed phase existing as particles, droplets, or bubbles. The governing equation for the continuous phase is based on the principle of mass conservation within a closed system [21].

2.4.1 Navier-stokes equation

$$\rho\left(\frac{\partial u}{\partial t} + u \cdot \nabla u\right) = -\nabla p + \mu \nabla^2 u + f \tag{2.7}$$

where, ρ is the fluid density, u is the velocity vector, t is time, p is the pressure, μ is the dynamic viscosity, ∇^2 is the Laplacian operator, and f represents external body forces (e.g., gravity). For an incompressible fluid, the continuity equation simplifies to:

$$\nabla \cdot u = 0. \tag{2.8}$$

2.4.2 Momentum equation (Navier-stokes equation)

This equation is derived from Newton's second law (the force-acceleration law) and represents the conservation and change of momentum in the continuous phase. For a Newtonian fluid, the Navier-Stokes equation is given by:

$$f + \mu \nabla^2 u + p\nabla - = \rho\left(\frac{u\partial}{t\partial} + (u.\nabla)u\right) \tag{2.9}$$

where, ρ is the fluid density, u is the velocity vector, p is the pressure, μ is the dynamic viscosity, and f is the volumetric force (such as gravitational force). This equation represents the balance of forces in an incompressible flow with a constant viscosity coefficient.

2.5 Heat transfer

To model heat transfer in a fluid using ANSYS Fluent, you need to first activate the energy equation and then set up the appropriate boundary conditions. In the given example, the inlet temperature to the chamber is $T_{inlet} = 300K$, and the walls are considered adiabatic (no heat transfer).

2.6 Other accelerations

Depending on the conditions, various forces, and consequently different accelerations, can act on a particle. In modeling the chamber, two additional forces are considered, which are discussed below.

2.6.1 Brownian force

The impact of Brownian motion, which is typically significant for submicron particles, can be included in the force balance on the particle. The acceleration due to this force is given by:

$$a_{bi} = \delta_i \sqrt{\frac{\pi s_0}{\Delta T}} \tag{2.10}$$

In this context, δ represents the stochastic nature of Brownian motion, and S characterizes the strength of the Brownian force acting on the particle.

$$s_0 = \frac{216 v k_B T}{\pi^2 p d_p^5 (\frac{p_p}{p}) C_c} \tag{2.11}$$

In the equation above, v is the kinematic viscosity of the fluid, and k_B is the Boltzmann constant.

2.6.2 Saffman lift force

The Saffman lift force, which acts on particles in a fluid flow, is considered as a selective force impacting the motion of particles. This force is significant for small particles (typically submicron) and affects their dynamics in a flow. The acceleration due to the Saffman lift force can be expressed as follows [11]:

$$a_{L(saff)} = 1.615 \frac{p v^{\frac{1}{2}} d_p^2}{m_p} \left(u_i - u_{pi}\right) \left| \frac{du_i}{du_i} \right| sgn\left(\frac{du_i}{dx_i}\right) \tag{2.12}$$

where:

ρ: is the fluid density,

v: is the kinematic viscosity of the fluid,

d_p: is the particle diameter,

m_p: is the mass of the particle,

$\frac{du_i}{du_i}$: is the velocity gradient,

sgn: is the sign function.

2.7 Dispersed phase boundary conditions

This study examines particle behavior when interacting with walls under two boundary conditions:

Trap Condition: Particles are considered trapped upon first contact with the wall, used when particle deposition is of interest.

Reflection Condition: Particles are reflected away from the wall upon contact, used when deposition is not of interest.

The number of incoming particles matches the grid resolution at the inlet, and the particles are assumed to have the same temperature and velocity as the incoming fluid.

2.8 Turbulence modeling

To enhance the averaged governing equations for continuity, momentum, and energy, Reynolds stresses and turbulence fluxes are included. The Navier-Stokes equations, a comprehensive model for turbulent fluid flows, are typically solved using numerical methods due to their analytical complexity. In turbulence modeling, these equations are applied using the Reynolds-Averaged Navier-Stokes (RANS) method, which separates flow quantities into mean and fluctuating components [16]. For instance, velocity is divided into its mean and fluctuating parts.

$$ {}_i^{\prime}u + \overline{iu} = iu \tag{2.13}$$

iu: Instantaneous velocity component in the i-th direction.

$\overline{iu}$: Mean velocity component in the in the i-th direction.

${}_i^{\prime}u$: Fluctuating component of the velocity in in the i-th direction.

By substituting these components into the Navier-Stokes equations and applying averaging, we obtain the Reynolds-Averaged Navier-Stokes (RANS) equations. These equations include Reynolds stresses, which account for the turbulent fluctuations as an additional stress in the flow [19]. The Reynolds stresses are expressed as:

$$\tau_{ij}^{Re} = \rho \left(\overline{u_i' u_j'} \right) \tag{2.14}$$

where:

τ_{ij}^{Re}: represents the Reynolds stress tensor component

ρ: is the fluid density,

$\overline{u_i' u_j'}$: is the mean value of the product of the fluctuating velocity components

2.8.1 Model $k - \varepsilon$

The two-equation $k - \varepsilon$ turbulence model includes transport equations for turbulent kinetic energy (k) and turbulence dissipation rate (ε). It is effective for internal flows with small pressure gradients, providing accurate results without requiring mesh refinement near walls due to its advanced wall function approach.

$$\frac{\partial}{\partial t}(\rho K) + \frac{\partial}{\partial x_i}(\rho K U) = \frac{\partial}{\partial x_i}\left[\left(\mu + \frac{\mu_t}{\sigma_k}\right)\frac{\partial k}{\partial x}\right] + G_k + G_b - \rho\varepsilon \tag{2.15}$$

$$\mu_t = C_\mu \rho \frac{K^2}{\varepsilon} \tag{2.16}$$

In the $k - \varepsilon$ turbulence model equations provided earlier:

G_k: represents the production of turbulent kinetic energy due to the mean velocity gradient.

G_b: represents the production of turbulent kinetic energy due to buoyancy forces.

The constants used in the model are:

C_μ: which is typically around 0.09,

$C\epsilon1$ and $C\epsilon2$, which are generally 1.44 and 1.92, respectively.

2.8.2 Forces on the particles

To study particle transfer and movement from Algrange's perspective, Newton's second law states that the sum of all forces acting on a particle equals its inertia. In this context, the drag force is represented by F_D, while F represents other forces per unit mass applied to the particle in various directions.

$$\frac{du_P}{dt} = F_D \left(u + u_p\right) + \frac{g(\rho_P - \rho)}{\rho_P}. \tag{2.17}$$

2.8.3 Gravitational and buoyancy forces

The gravitational and buoyancy forces acting on a particle are defined by Equation (2.18) [16]. In this equation, g_i represents the gravitational force, while $\rho_p/gi(\rho)$ are related to the buoyancy force. The buoyancy force acts in the direction opposite to the gravitational force on the particle. Since the fluid density is negligible compared to the particle's density, this force is often very small and can generally be disregarded.

$$F_g = g_i \frac{4\pi r^3}{3} \left(\rho_P - \rho\right). \tag{2.18}$$

2.8.4 Drag force

When an object moves through a fluid in which it is immersed, a force proportional to the fluid's resistance and the relativemotion of the object is exerted. When a particle is suspended in a fluid, a force acts along the direction of movement or opposite to it. This force is known as the drag force. For low Reynolds numbers, the drag force on a spherical particle is determined by Stokes law, given by the following equation:

$$F_D = 3\pi\mu \left(u^f - u^p\right) d_p. \tag{2.19}$$

In the above equation, u^p represents the velocity of the particle, μ is the dynamic viscosity of the fluid, and d_p is the diameter of the particle. The fluid velocity, u^f, consists of both a mean component u^f and an instantaneous component u^f.

2.8.5 Thermophoretic force

A temperature gradient can induce motion of particles suspended in a fluid, resulting in the particle experiencing a force in the direction of decreasing temperature. This motion of particles due to the temperature gradient is known as thermophoresis. This force is distinct from the forces resulting from the temperature gradient between surfaces and airflow, which cause fluid movement and particle transport due to the movement of the fluid [13]. The thermophoretic force acts directly on the particles through the temperature gradient and depends on the properties of both the particle and the fluid, as well as the temperature gradient.

$$F_t = \frac{9\pi\mu^2 d\nabla T}{4\rho_m T} \left(\frac{1}{1 + \frac{k_p}{2k_m}}\right) \tag{2.20}$$

$$F_t = \frac{1}{2}\frac{\pi\mu v d^2}{\lambda T}\nabla. \tag{2.21}$$

2.9 Ground coil system

Phase 1 of the project involved the design and installation of the ground coil system, including drilling, piping, and grouting. Given the climatic conditions and ground temperature, the ground coil was designed as a closed vertical system, where the heat transfer fluid, a mixture of water and a percentage of ethylene glycol, circulates between the coil and the heat exchanger. The ground coil pipes, which connect the heat transfer fluid to the ground, need to have high durability, pressure resistance, adequate heat transfer, and low thermal loss [18]; therefore, high-pressure polyethylene pipes were used.

2.10 Equipment specifications

The main equipment used in this system includes fan coils, pumps for the ground coil circuit and the building's internal circuit, and a heat pump. These components form the core of a geothermal system.

2.10.1 Fan coils

Based on the thermal load and cooling calculations, 12 fan coils with capacities of 400 and 600 cubic feet per minute were specified to meet the building's requirements. After thorough research, fan coils with the following specifications were purchased.

Table 3: Technical Specifications of the Installed Fan Coils in the Building

Model	brand	number	Air flow rate (cubic feet per minute)
SA-FC-400	Sabafarin	6	400
SA-FC-600	Sabafarin	6	600

2.10.2 Pump specifications

Based on the flow rate of the circulating fluid in the ground coil circuit and the distribution system, Grundfos circulator pumps have been purchased. To minimize the risk of system downtime, two circulator pumps have been selected for each circuit. The models of these pumps have been determined according to the flow rate and pressure drop of each line. Their specifications are provided in the table below.

Table 4: Technical Specifications of the Pumps

Title	Flow Rate (Gallons per Minute)	Head (Meters)	Quantity	Model
Ground Coil Model	30	22	2	TP 40-270/2
Distribution Circuit	20	20	2	CM 5-3
Domestic Hot Water	4	7	1	UPS 25-80

2.11 Boundary conditions

To achieve optimal results, the appropriate definition of boundary conditions is essential. According to Figure 1, the boundary condition at the inlet is defined as the inlet velocity, and at the outlet, the condition is defined as the outlet flow. The surrounding environmental conditions are defined as symmetric, and the air pressure is assumed to be uniform across all models.

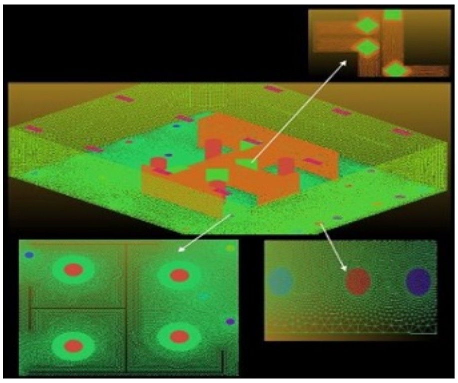

Figure 1: Mesh Configuration Used for the Chamber, Vents, Computers, and Personnel

2.12 Validation

To ensure the accuracy of various models and to reduce the uncertainty caused by different numerical methods in solving the continu ity and momentum equations, validation is essential. In this study, the work of Li et al. has been used for the validation of flow and particle transport. The geometry employed is a simple chamber with dimensions of $0.4 \times 0.8 \times 0.4$ meters. The inlet and outlet vents, with dimensions of 0.04×0.04 meters, are positioned at distances of 36 and 4 centimeters from the central plane, respectively. The inlet velocity is considered to be 0.225 meters per second, and the outlet pressure is set to zero relative pressure. A no-slip boundary condition has been applied to all walls.

3 Findings

Given previous research on the impact of suspended particles on health and thermal comfort, a better understanding of HVAC systems is essential for improving indoor conditions. Initially, various turbulence models were examined for validating fluid flow, and the most suitable model was selected based on solution accuracy and convergence time.

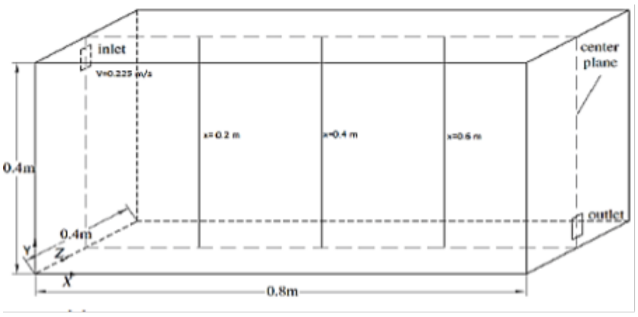

Figure 2: shows the geometry used and the measurement points at distances located in the mid-plane

Subsequently, particle flow was analyzed and validated using the selected model in a laboratory setup to prepare it for application under current conditions.

3.1 Results of the continuous phase

By solving the governing equations for flow and temperature, particle trajectories are determined. The flow and temperature equations are iteratively solved to achieve the desired accuracy, with convergence criteria guiding the precision. FLUENT software displays residual values to indicate solution errors. In Figure 3, the graph of changes in the velocity component in the x direction at the distance between the inlet tip and the panel is shown.

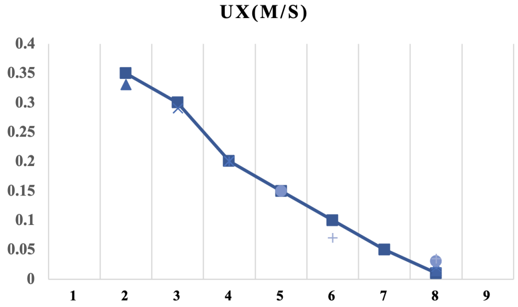

Figure 3: illustrates the variations of the velocity component in the x-direction across the distance between the inlet and the cylinder

In Figure 4, the pressure distribution within the chamber is depicted in a sectional view. A close examination of this figure reveals that the relative pressure across the entire computational domain is approximately 14,000 Pascals, which corresponds to the pressure within the outlet suction cavity.

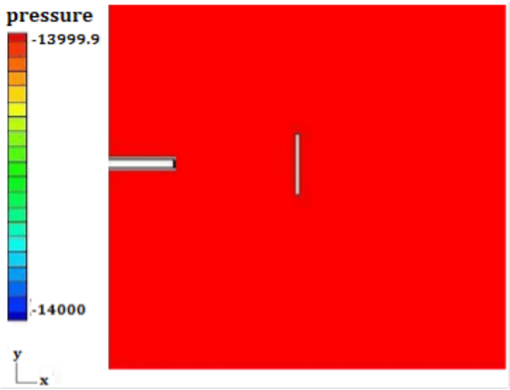

Figure 4: illustrates the pressure distribution in a cross-section of the chamber

As shown in Figure 5, the velocity at the inlet starts at 0.32 meters per second and gradually increases until it reaches a maximum point. The velocity then gradually decreases, eventually reaching zero at the wall. This slight and noticeable increase in velocity from the initial 0.32 meters per second is due to the suction effect at the outlet, which can be observed in the region between the inlet and the panel. To ensure the accuracy of the results, the velocity profiles in the x-direction (ux) along three vertical axes at different distances from the inlet tip were compared with the findings of Sha et al. In the figure below, the vertical axes are shown, and the distances from the inlet tip to these axes are 10, 20, and 25 millimeters, respectively.

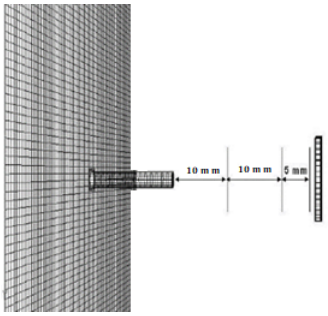

Figure 5: Three vertical axes for comparison with the study [1]

The results of this validation are presented in Figure 6.

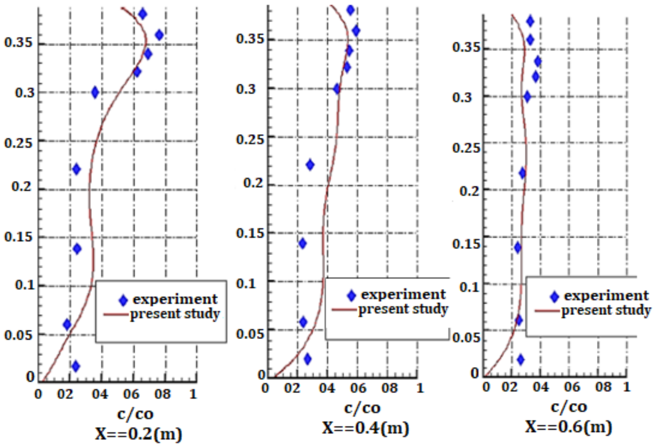

Figure 6: Normalized concentration validation results graph

In the figure 6, the vertical axis is non-dimensionalized using the inlet velocity of the computational domain (in this study, $u_{inlet} = 0.32m/s$), and the horizontal axis is non-dimensionalized with the panel length (in this study, 13.2 mm). The slight differences between the velocity profiles can be attributed to variations in the meshing approach between this study and the research by Sha and colleagues. In Sha et al.'s study, the computational domain was meshed with 1,200,000 unstructured hybrid cells, whereas this simulation used 940,000 structured cells, which has led to computational cost savings and improved result accuracy.

3.2 Results of the discrete phase

3.2.1 Constant density for the fluid

After solving the flow and energy equations, the next step involves particle injection. Once the particles enter the chamber, they are subjected to various forces. In this simulation, the primary particle diameter considered is 1 micron, although different diameters are also examined to study size effects. The main forces acting on the particles include drag, gravity, and thermophoresis, while lift and Brownian effects are considered secondary forces. The impact of these and other factors on particle deposition on the panel has been analyzed, and the results are presented subsequently.

3.2.2 Forces involved: Drag, gravity, and thermophoresis

As mentioned in the previous chapter, four different temperature boundary conditions were considered. It is important to note that, except for the two isothermal walls, all other walls were assumed to be adiabatic. The deposition of 1-micron particles from the airflow under these boundary conditions on the panel is shown in Figure 7 for each scenario.

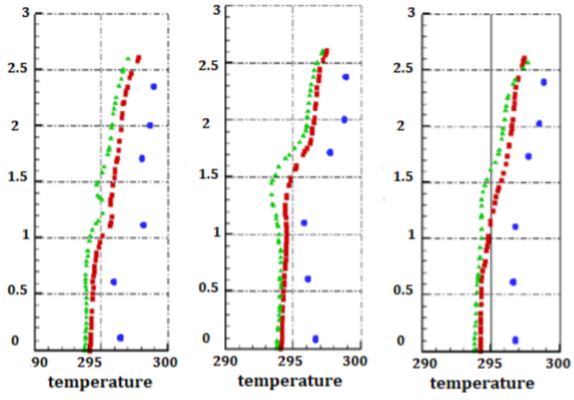

Figure 7: shows the temperature curves as a function of height for points under different boundary conditions

In the figure 7, the vertical axis represents the deposition fraction, which indicates the ratio of particles deposited on the panel to the total number of incoming particles. The number of incoming particles is equivalent to the mesh density of the inlet plane. It is evident that the effect of thermophoresis manifests as differences in deposition fractions under various temperature conditions, since weight and drag forces are considered in both cases. It is observed that temperature differences at heights between 0.1 and 1.1 meters around the thermal simulators are less than 1.5°C, and in some cases, do not exceed 1°C. In contrast, at higher elevations above 1.1 meters, the temperature difference has a more pronounced effect.

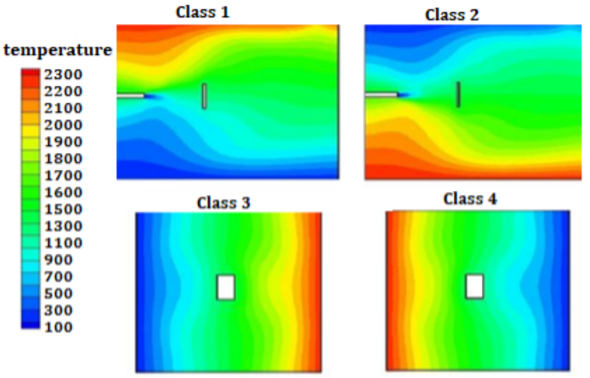

Figure 8: shows the temperature distribution under the assumed boundary conditions

As observed, thermal forces are considered relatively weak. Figure 8 aids in better understanding the temperature distributions under the assumed conditions. Given that the third scenario is identified as the most effective for particle deposition, the subsequent simulations will be based on this condition. The impact of thermophoresis on particles, shown through its effect on particle concentration distribution near the panel, is illustrated in Figure 9. It is evident that in the presence of a temperature gradient, the particle distribution shifts toward the cooler wall.

To examine the effect of temperature on particle deposition, the temperature difference between the left and right walls was increased. Specifically, the temperature of the left wall was kept constant at 300 K, while the temperature of the right wall was gradually increased. The impact of this change is illustrated in the figure 10.

According to Figure 10, the temperature at points 4PS, 3PS, 2PS, and 1PS around the cylindrical simulators is shown as a function of height. At each of these four points, the temperature increase up to a height of less than 1 meter is less than 1 Kelvin. However, occupants in areas 1S and 3S experience a temperature decrease of up to 1.5°C at heights between 1 and 1.5 meters due to the increased air velocity from nearby vents. Consequently, in this height range, occupants in areas 1S and 3S, being close to the air distribution vents, experience lower temperatures compared to those in areas 2S and 4S.

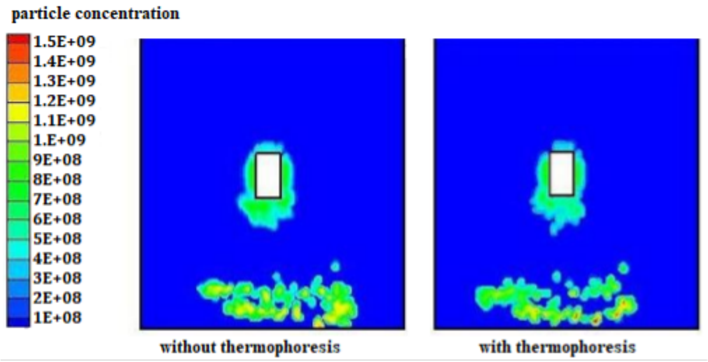

Figure 9: shows the variation in particle concentration distribution near the panel in the presence of a temperature gradient

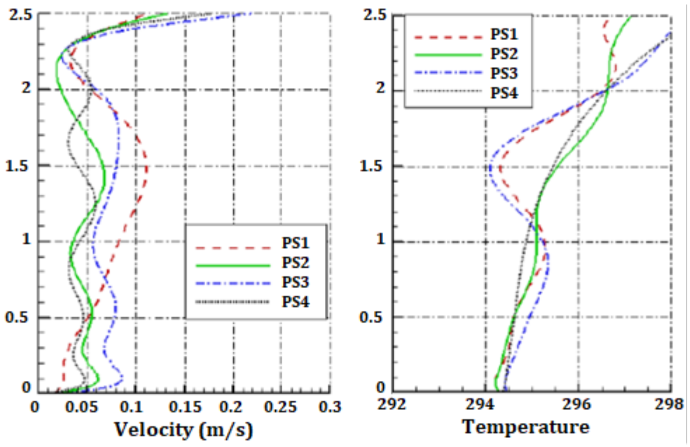

Figure 10: shows the curves of air velocity and temperature as a function of height for four points

3.3 Impact of lift and brownian forces

In this simulation, lift and Brownian forces are considered secondary (lateral) forces. The effects of these forces, along with the primary forces, on the deposition of 1-micron particles were examined. Additionally, particles of sizes 0.05, 0.1, and 10 microns were also studied. The results for three different inlet velocities are presented in Figure 11.

It is noteworthy that, as shown in the graphs, lateral forces significantly affect sub-micron particles. Specifically, for particle diameters of 1 and 10 microns, the green and red curves align with the black curve on the graph, which aligns well with reality. It is observed that thermophoretic force has the greatest impact on micron-sized particles. It is also important to mention that in all cases, drag and gravitational forces are present.

3.4 Simulation of particles entering through the ventilation system

After analyzing and simulating the flow parameters, the simulation of particles entering the chamber was conducted. The particles, with diameters ranging from 0.75 to 4 micrometers and a density of 2000 kg/m^3, were released from the beginning of the ventilation process, and their concentration gradually increased in the environment. Since this study focuses on simulating particles introduced by the ventilation system, which supplies air at 19.2°C for cooling purposes, it was assumed that the particles enter the environment at this temperature. Table (2-3) summarizes the characteristics of the released particles.

In simulations involving discrete phase particles, tracking more particles requires more memory and processing power, which naturally increases computational costs. To reduce these costs, the simulation was performed with three different particle release rates—33,000, 46,000, and 92,000 particles per second—and the concentration distribution in the working area was compared for these rates. The comparison of concentration contours for 46,000 and 92,000 particles per second showed that the difference between these rates is less than 8%. Therefore, a release rate of 46,000 particles per second was chosen for future computations.

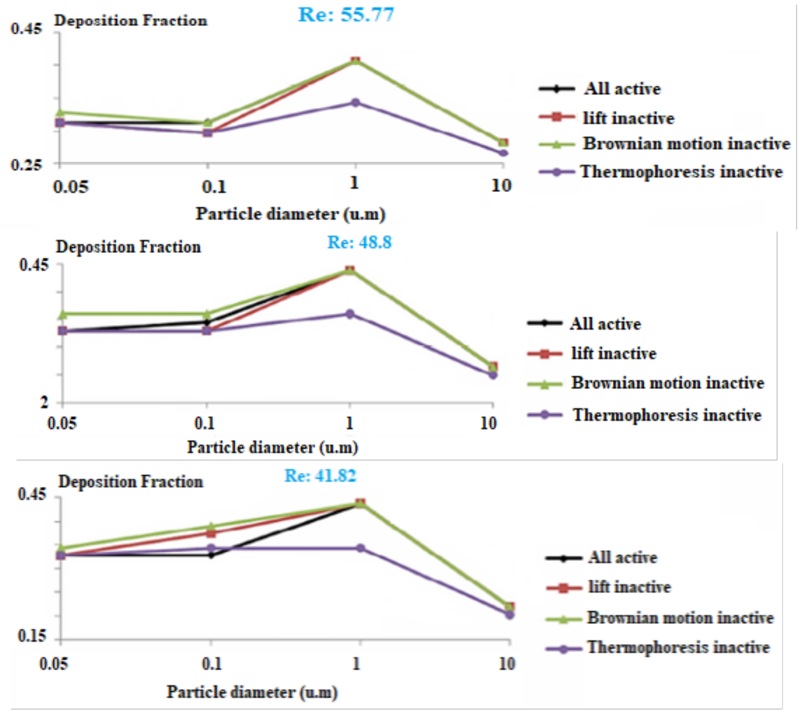

Figure 11: shows the impact of various forces on particle deposition at different inlet velocities

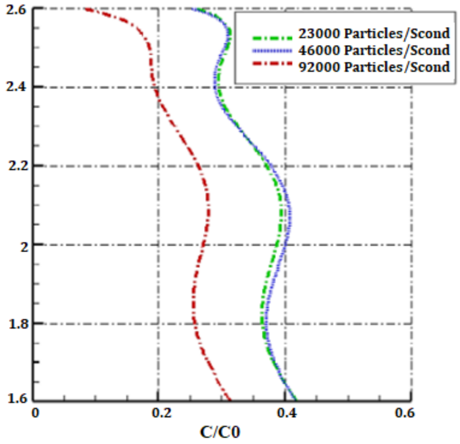

Figure 12: simulations involving discrete phase particles

After determining the appropriate particle release rate, the focus shifted to comparing the transport and deposition of particles with different sizes in the environment. At this stage, only the particle equations were analyzed, and the flow and energy equations were not solved. To achieve a steady state, the particle concentration remained constant in the internal environment after 982 seconds. During this period, particle concentrations in various room areas and the working area were examined, and the maximum values for 0.1 and 10-micron particles were extracted. Particles passing through the inlet pages and the central pages of the cylindrical simulators were also analyzed.

In areas beneath tables and medical equipment, and between tables and ventilation vents, particle concentrations are lowest due to thermophoresis, thermal plume effects, and flow deflection towards heat sources. Larger particles are more likely to settle in these regions, with gravitational forces significantly affecting 10-micron particles. These particles settle more at lower heights and on surfaces. Asymmetrical vents and geometric irregularities prevent uniform particle concentrations in the working area [10]. Additionally, 10-micron particles do not follow airflow in the spaces between thermal simulators and the operating table due to the table acting as a barrier.

The results indicate that 10-micron particles, due to gravitational forces, have a greater tendency to settle compared

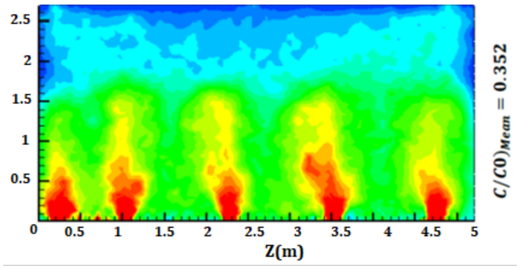

Figure 13: shows the normalized concentration of particles on the vertical plane at $x = 0.225$ (m)

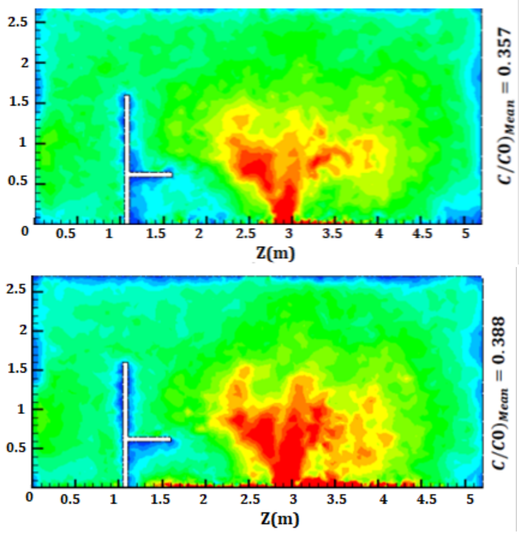

Figure 14: shows the normalized concentration of particles on the vertical plane at $x = 1.78$ m

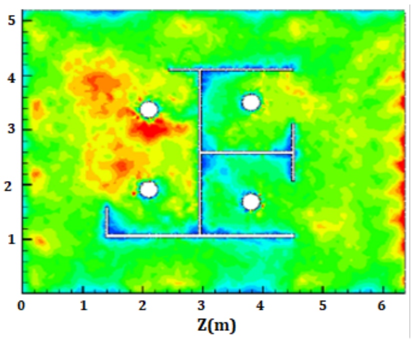

Figure 15: shows the normalized concentration of particles on the horizontal plane at $y = 1.1y$ meters

to smaller particles. Additionally, for cylindrical mannequins located near the inlet vents, although better temperature conditions are provided, the particle concentration in these areas is higher, which poses a health risk. In this HVAC system, particle concentration decreases with height, and smaller particles are more likely to exit the room.

4 Conclusion

This study found that heat sources in indoor spaces significantly impact airflow, a conclusion supported by both previous studies and current simulations. The analysis, which considered gravitational effects and particle-fluid interactions, showed that smaller particles are less likely to settle. Understanding particle transport and deposition is crucial due to their potential to enter the respiratory system. Simulations were validated against similar research, revealing that thermophoresis is a weak force but becomes more effective with greater temperature differences between walls, leading to increased particle deposition on cylinders [16, 17, 18, 19]. Adjusting cylinder position and orientation

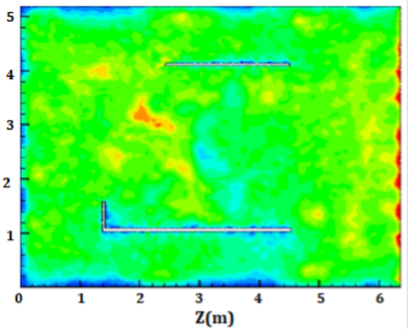

Figure 16: shows the normalized concentration of particles on the horizontal plane at $y = 1.6y = 1.6y = 1.6$ meters

also affected deposition, with optimal results achieved at a 55° angle relative to the initial position. At higher inlet velocities, drag force mainly governs particle deposition, while thermophoresis is more significant at medium velocities. Lift and Brownian forces have a minor impact on deposition but affect submicron particles. Introducing a Boussinesq fluid demonstrated that increased fluid compressibility enhances particle deposition due to greater convective contribution. The analysis shows that the system effectively removes airborne pollutants, clearing the environment of particles about 240 seconds after injection stops.

It achieves high efficiency in removing pollutants of various sizes, with a 90% reduction in particle concentrations measured over time on both planar and linear scales. This study examined airflow velocity, temperature, and particle behavior in an office with various heat sources and a modern HVAC system with rotating floor diffusers. It confirmed that indoor heat sources significantly affect airflow, as supported by previous and current simulations. Although gravitational effects and bidirectional particle-fluid interactions were not analyzed, the study found that smaller particles are less likely to settle. Understanding the transport and deposition of these particles, which can penetrate the respiratory system, is essential. The study analyzed particle movement in an indoor space, focusing on concentrations in work areas and airflow entry points. It was found that 10-micron particles tend to stay near the ground, while 12-micron particles have higher average concentrations at lower elevations compared to 0.1-micron particles. Larger particles generally settle more due to gravity. The study also examined normalized particle concentrations in the breathing zone and areas behind individuals, finding that cylindrical simulator 1s, despite optimal thermal conditions, had the highest particle concentration in the breathing zone due to its proximity to air distribution vents, whereas simulator 4s had the lowest exposure.

References

[1] A.E. Andersson, I. Bergh, J. Karlsson, B.I. Eriksson, and K. Nilsson, *Traffic flow in the operating room: an explorative and descriptive study on air quality during orthopedic trauma implant surgery*, Amer. J. Infect. Control **40** (2012), no. 8, 750–755.

[2] M.K. Annaqeeb, Y. Zhang, J.W. Dziedzic, K. Xue, C. Pedersen, and L.I. Stenstad, … and G. Cao, *Influence of surgical team activity on airborne bacterial distribution in the operating room with a mixing ventilation system: A case study at St. Olavs Hospital*, J. Hospital Infect. **116** (2021), no. 6, 91–98.

[3] J. Bao and J. Li, *The effect of type of ventilation used in the operating room and surgical site infection: A meta-analysis*, Infect. Control Hospital Epidemiol. **42** (2021), no. 8, 931–936.

[4] Y. Bi, A. Aganovic, H.M. Mathisen, and G. Cao, *Experimental study on the exposure level of surgical staff to SARS-CoV-2 in operating rooms with mixing ventilation under negative pressure*, Build. Envir. **217** (2022), 109091.

[5] J.K. Calautit, P.W. Tien, S. Wei, K. Calautit, and B. Hughes, *Numerical and experimental investigation of the indoor air quality and thermal comfort performance of a low energy cooling windcatcher with heat pipes and extended surfaces*, Renew. Energy **145** (2020), no. 2, 744–756.

[6] G. Cao, I. Kvammen, T.A.S. Hatten, Y. Zhang, L.I. Stenstad, G. Kiss, and J.G. Skogas, *Experimental measurements of surgical microenvironments in two operating rooms with laminar airflow and mixing ventilation systems*, Energy Built Envir. **2** (2021), no. 2, 149–156.

[7] A.C. D'Alicandro and A. Mauro, *Effects of operating room layout and ventilation system on ultrafine particle transport and deposition*, Atmospher. Envir. **270** (2022), 118901.

[8] V. Gholami Motlagh, M. Ahmadzadehtalatapeh, and O. Mohammadi, *Effect of turbulent and laminar flow mechanisms on air flow patterns and CO2 distribution in an operating room: A numerical analysis abbreviated title: Air flow pattern in an operating room*, Sci. Iran. **30** (2023), no. 3, 1008–1026.

[9] K. Khankari, *Hospital operating room ventilation systems*, ASHRAE J. **60** (2018), no. 6, 16–26.

[10] H. Langvatn, J. C. Schrama, G. Cao, G, Hallan, O. Furnes, E. Lingaas, and H. Dale, *Operating room ventilation and the risk of revision due to infection after total hip arthroplasty: Assessment of validated data in the Norwegian Arthroplasty Register*, J. Hospital Infect. **105** (2020), no. 2, 216–224.

[11] J.R. Lewis, *Operating room air distribution effectiveness*, ASHRAE Trans. **99** (1993), no. 2, 1191–1199.

[12] Z. Liu, M. Zhang, G. Cao, S. Tang, H. Liu, and L. Wang, *Influence of air supply velocity and room temperature conditions on bioaerosols distribution in a class I operating room*, Build. Envir. **204** (2021), 108116.

[13] M.D.A. Melhado, J.L.M. Hensen, and M.G.L.C. Loomans, *Review of Operating Room Ventilation Standards*, 17th Int. Air-condition. Ventil. Conf., Prague STP - Society of Environmental Engineering, 2006.

[14] M. Niu, H. Chen, J. Liu, C.H. Tseng, J. Shin, N. Hoftman, and Y. Zhu, *Effects of operating room ventilation on particle exposure and removal during general endotracheal anesthesia*, J. Build. Engin. **84** (2024), 108596.

[15] X. Ouyang, Q. Wang, X. Li, T. Zhang, and S. Rastogi, *Laminar airflow ventilation systems in orthopaedic operating room do not prevent surgical site infections: a systematic review and meta-analysis*, J. Orthop. Surgery Res. **18** (2023), no. 1, 572–585.

[16] M. L. Pereira and A. Tribess, *A review of air distribution patterns in surgery rooms under infection control focus*, Engenharia Térmica=Thermal Engin. **4** (2005), no. 2, 113–121.

[17] S. Sadrizadeh, A. Aganovic, A. Bogdan, C. Wang, A. Afshari, A. Hartmann and G. Cao, *A systematic review of operating room ventilation*, Journal of Building Engineering **40** (2021), 102693.

[18] B. Surial, A. Atkinson, R. Külpmann, A. Brunner, K. Hildebrand, B. Sicre, and J. Marschall, *Better operating room ventilation as determined by a novel ventilation index is associated with lower rates of surgical site infections*, Ann. Surgery **276** (2022), no. 5, 353–360.

[19] A. Tammelin, P. Kylmänen, and A. Samuelsson, *Comparison of number of airborne bacteria in operating rooms with turbulent mixing ventilation and unidirectional airflow when using reusable scrub suits and single-use scrub suits*, J. Hospital Infect. **135** (2023), no. 10. 119–124.

[20] D. Von Wedel, S. Redaelli, A. Suleiman, L.J. Wachtendorf, M. Fosset, P. Santer, and M.S. Schaefer, *Adjustments of Ventilator Parameters during Operating Room–to–ICU Transition and 28-Day Mortality*, Amer. J. Respirat. Critic. Care Med. **209** (2024), no. 5, 553–562.

[21] C. Wang, S. Holmberg, and S. Sadrizadeh, *Numerical study of temperature-controlled airflow in comparison with turbulent mixing and laminar airflow for operating room ventilation*, Build. Envir.**144** (2018), no. 8, 45–56.

[22] Y. Wang, J. Tang, Z. Pan, and C. Yan, *Particle swarm optimization-based planning and scheduling for a laminar-flow operating room with downstream resources*, Soft Comput. **19** (2015), no. 4, 2913–2926.

[23] M. Ziegler, H.M. Seipp, T. Steffens, D. Walter, K. Büttner-Janz, D. Rodger, and J. Herzog-Niescery, *Infection prevention and the protective effects of unidirectional displacement flow ventilation in the turbulent spaces of the operating room*, HERD: Health Envir. Res. Design J. **25** (2024), no. 6.